

Exact Diagonalization Dynamical Mean Field Theory for Multi-Band Materials: Effect of Coulomb correlations on the Fermi surface of $\text{Na}_{0.3}\text{CoO}_2$

C.A. Perroni,¹ H. Ishida,² and A. Liebsch¹

¹*Institut für Festkörperforschung, Forschungszentrum Jülich, 52425 Jülich, Germany*

²*CREST, JST, and College of Humanities and Sciences,
Nihon University, Sakura-josui, Tokyo 156, Japan*

Dynamical mean field theory combined with finite-temperature exact diagonalization is shown to be a suitable method to study local Coulomb correlations in realistic multi-band materials. By making use of the sparseness of the impurity Hamiltonian, exact eigenstates can be evaluated for significantly larger clusters than in schemes based on full diagonalization. Since finite-size effects are greatly reduced this approach allows the study of three-band systems down to very low temperatures, for strong local Coulomb interactions and full Hund exchange. It is also shown that exact diagonalization yields smooth subband quasi-particle spectra and self-energies at real frequencies. As a first application the correlation induced charge transfer between t_{2g} bands in $\text{Na}_{0.3}\text{CoO}_2$ is investigated. For both Hund and Ising exchange the small e'_g Fermi surface hole pockets are found to be slightly enlarged compared to the non-interacting limit, in agreement with previous Quantum Monte Carlo dynamical mean field calculations for Ising exchange, but in conflict with photoemission data.

I. INTRODUCTION

Dynamical mean field theory (DMFT)¹ has been used successfully during recent years to describe the electronic properties of a variety of strongly correlated materials.² The hallmark of these systems are their complex lattice geometries, giving rise to intricate single-particle properties, accompanied by complex many-electron interactions in partially filled, nearly localized atomic orbitals. These characteristics lead to a wealth of physical phenomena such as metal insulator transitions, exotic magnetic structures and unconventional superconducting phases.³ The virtue of DMFT is that it treats single-electron and many-electron features on the same footing. The key conceptual advance of this approach is the mapping of the lattice problem onto an effective impurity problem which is solved numerically exactly. The local self-energy is then determined via a self-consistency procedure.

The many-body impurity problem can be solved, in the case of single-band systems, by using techniques such as numerical renormalization group⁴ (NRG), exact diagonalization⁵ (ED), quantum Monte Carlo⁶ (QMC), or other schemes.¹ For computational reasons dynamical correlations in realistic multi-band materials have so far been investigated mainly within QMC², iterated perturbation theory⁷ (IPT) and the fluctuation exchange method⁸ (FLEX). The versatility of the QMC approach is made feasible by allowing only for Ising-like exchange interactions to avoid serious sign problems at low temperatures.⁹ Extensions of QMC including full Hund's exchange are presently limited to $T = 0$ ¹⁰ and rather high temperatures ($T > 1500$ K).¹¹ Spin-flip interactions at low finite temperatures can be taken into account in two recently developed schemes, namely, the continuous-time QMC method^{12,13} and the combination of the Hirsch-Fye algorithm with a perturbation series expansion.¹⁴

The aim of this work is to demonstrate that multi-

band ED/DMFT is a highly useful scheme for the investigation of Coulomb correlations in realistic materials. In the past, applications of ED/DMFT were limited to one-band and two-band systems because of the extremely rapid increase of the Hilbert space when the size n_s of the cluster used to simulate the solid is enlarged.^{15,16,17} For instance, ED with two impurity orbitals, each coupled to three bath levels ($n_s = 8$), requires diagonalization of matrices with dimension up to 4900 which roughly represents the time and storage limit of what is computationally meaningful.¹⁸ We show here that a considerable simplification of this task can be achieved by exploiting the extreme sparseness of the Hamiltonian matrices and focusing on the limited number of excited states relevant at low temperatures. As a result the cluster size $n_s = 12$ can be treated at about the same computational cost as full diagonalization for $n_s = 8$. This improvement allows for the first time the application of ED/DMFT to realistic three-band systems.

In this work we study the intercalated layer compound Na_xCoO_2 which exhibits an unusual range of electronic properties as a function of Na doping: unconventional superconductivity, magnetic and charge ordering, and metal insulator transition. Here we focus on one of the most puzzling and controversial aspects, namely, the topology of the Fermi surface at $x = 0.3$, the Na concentration at which the system becomes superconducting when additionally doped with water.¹⁹ As a result of the octahedral crystal field, the Co $3d$ bands are split into t_{2g} and e_g subbands separated by a finite energy gap. With Na doping the filling of the t_{2g} bands can be continuously tuned between $n = 5$ and $n = 6$. The rhombohedral symmetry at Co sites yields a further splitting of t_{2g} orbitals into an a_g and two doubly degenerate e'_g orbitals. According to density functional theory within the local density approximation (LDA) the Fermi surface consists of a large a_g hole surface centered at Γ and six small e'_g hole pockets along the ΓK directions.²¹ At $x = 0.3$ the 0.7

holes in the t_{2g} band consist of about 0.4 a_g holes and 0.3 e'_g holes. Thus, both types of states should be important for a variety of electronic and magnetic properties.

In striking contrast to these LDA predictions, angle-resolved photoemission spectroscopy (ARPES) experiments reveal only the large a_g Fermi surface, the e'_g bands being completely filled.²² To resolve this discrepancy several possible explanations have been discussed in the literature. Since the onsite Coulomb energy U among Co 3d electrons is about twice the width of the t_{2g} bands a correlation induced inter-orbital charge transfer among t_{2g} states could in principle modify the shape of the Fermi surface. Dynamical correlations evaluated within multi-band QMC/DMFT for a realistic single-particle Hamiltonian predict slightly enlarged e'_g Fermi surface pockets.²³ The same trend was found in recent QMC/DMFT calculations.^{24,25} On the other hand, accounting approximately for band narrowing via the Gutzwiller approach, filled e'_g bands were obtained in the strong-coupling $U \rightarrow \infty$ limit,²⁶ but these calculations have not yet been extended to realistic values of U and finite exchange integrals J .

The role of the intercalated Na atoms has also been studied. Within LDA, disorder in the Na layer was shown to produce potential variations that can localize the e'_g Fermi surface pockets, at least for large doping.²⁷ A recent LDA+QMC/DMFT study of Na disorder also showed that the pockets are likely to disappear at large x , but to remain stable near $x = 0.3$.²⁵

Although the QMC/DMFT results^{23,24,25} so far represent the most accurate analysis of correlation induced modifications of the Fermi surface of $\text{Na}_{0.3}\text{CoO}_2$, they are limited to Ising exchange because of the QMC sign problems alluded to above. Since the e'_g bands reach only about 100 meV above the Fermi level – an energy much smaller than typical exchange integrals – there arises the question to what extent the inclusion of full Hund's exchange might provide an explanation of the observed ARPES data.

To address this issue we have applied ED/DMFT to $\text{Na}_{0.3}\text{CoO}_2$. The important result of the present work is that dynamical on-site correlations within the Co t_{2g} manifold for realistic values of Coulomb and exchange energies give rise to a transfer of electronic charge from the e'_g bands to the a_g band. For Hund's exchange and $T = 10$ meV the number of a_g holes is decreased to 0.351 compared to the LDA value 0.40, while the number of e'_g holes is increased to 0.349 from the LDA value 0.30. Nearly identical values are found for Ising exchange: 0.345 (a_g) and 0.355 (e'_g). These results are qualitatively consistent with previous QMC/DMFT calculations for Ising exchange at $T = 30 \dots 60$ meV. Local Coulomb correlations can therefore be ruled out as a possible explanation of the absence of the e'_g hole pockets in the ARPES data.

It remains to be investigated experimentally and theoretically to what extent the photoemission data are influenced by surface effects which have played a cru-

cial role also in other transition metal oxides, such as Sr_2RuO_4 and $\text{Sr}_x\text{Ca}_{1-x}\text{VO}_3$. Also, we note that the present ARPES results do not seem to be consistent with recent Shubnikov-de Haas measurements of the Fermi surface of $\text{Na}_{0.3}\text{CoO}_2$.³³

The present work establishes multi-band ED/DMFT as a useful scheme for describing strongly correlated materials. In this sense ED/DMFT can now be regarded as complementary to multi-band QMC/DMFT. In comparison to standard Hirsch-Fye QMC treatments, important advantages of ED/DMFT are that spin-flip and pair-exchange interactions are fully taken into account, large Coulomb energies pose no computational problems, and temperatures as low as 5 to 10 meV are readily accessible.

The outline of this paper is as follows. In Section II we present the main ingredients of the multi-band ED/DMFT approach. We also argue that it is possible within this scheme to evaluate continuous spectral functions and self-energies at real frequencies for the extended material. Section III presents the application to $\text{Na}_{0.3}\text{CoO}_2$ where we focus on the correlation induced charge transfer among the partially filled t_{2g} bands. Summary and Outlook are given in Section IV.

II. THEORY

A. Multi-band ED/DMFT

Let us consider a material whose single-particle properties are characterized by a Hamiltonian $H(\mathbf{k})$. In the case of partially occupied t_{2g} bands of a transition metal oxide such as Na_xCoO_2 , $H(\mathbf{k})$ is a 3×3 matrix whose elements account for direct interactions between t_{2g} orbitals as well as indirect interactions via neighboring Oxygen ions. In addition we consider on-site Coulomb interactions which are comparable to or larger than the t_{2g} band width. The purpose of single-site DMFT is to derive a local self-energy $\Sigma(\omega)$ which describes the modification of the single-particle bands caused by Coulomb interactions. The local lattice Green's function is then given by the expression

$$G_{\alpha\beta}(i\omega_n) = \sum_{\mathbf{k}} \left(i\omega_n + \mu - H(\mathbf{k}) - \Sigma(i\omega_n) \right)^{-1}_{\alpha\beta} \quad (1)$$

where $\omega_n = (2n+1)\pi/k_B T$ are Matsubara frequencies, μ is the chemical potential, and $\alpha, \beta = d_{xy}, d_{xz}, d_{yz}$ denotes the t_{2g} orbital basis. We consider paramagnetic systems and omit the spin index of Green's functions and self-energies for convenience.

In the case of a two-dimensional hexagonal lattice, local quantities such as $G_{\alpha\beta}(i\omega_n)$ have only two independent elements given by $G_{11} = G_{22} = G_{33}$ and $G_{12} = G_{13} = G_{23}$. It is therefore convenient to go over to the a_g, e'_g basis, where $a_g = (d_{xy} + d_{xz} + d_{yz})/\sqrt{3}$, $e'_{g1} = (d_{xy} + d_{xz} - 2d_{yz})/\sqrt{6}$ and $e'_{g2} = (d_{xy} - d_{xz})/\sqrt{2}$.

Within this basis G becomes diagonal, with elements

$$G_{m=1} \equiv G_{a_g} = G_{11} + 2G_{12} \quad (2)$$

$$G_{m=2,3} \equiv G_{e'_g} = G_{11} - G_{12}. \quad (3)$$

The reverse transformation is $G_{ii} = (G_{a_g} + 2G_{e'_g})/3$ and $G_{ij} = (G_{a_g} - G_{e'_g})/3$. Except for the Brillouin Zone integral in Eq. (1) we perform all subsequent calculations in the diagonal a_g, e'_g basis denoted by $m = 1 \dots 3$. Analogous transformations hold for other lattice structures, such as square two-dimensional or cubic three-dimensional systems.

For the purpose of the quantum impurity calculation it is necessary to first remove the self-energy from the central site. This step yields the impurity Green's function

$$G_{0,m}(i\omega_n) = [G_m(i\omega_n)^{-1} + \Sigma_m(i\omega_n)]^{-1}. \quad (4)$$

Note that, since G_m , $G_{0,m}$ and Σ_m characterize the extended solid, they have smooth, continuous spectra at real frequencies.

Within ED/DMFT⁵ the lattice impurity Green's function $G_{0,m}$ is approximated via an Anderson impurity model for a cluster consisting of impurity levels $\varepsilon_{m=1\dots 3}$ and bath levels $\varepsilon_k = 4 \dots n_s$ coupled via hopping matrix elements V_{mk} . Thus,

$$G_{0,m}(i\omega_n) \approx G_{0,m}^{cl}(i\omega_n) \quad (5)$$

where

$$G_{0,m}^{cl}(i\omega_n) = \left(i\omega_n + \mu - \varepsilon_m - \sum_{k=4}^{n_s} \frac{|V_{mk}|^2}{i\omega_n - \varepsilon_k} \right)^{-1}. \quad (6)$$

Here, $n_s = 12$ is the cluster size used in the calculations discussed below. Since $G_{0,m}^{cl}$ is diagonal in orbital indices, each impurity level couples to its own bath containing three levels. Evidently, in contrast to $\text{Im } G_{0,m}$, at real ω $\text{Im } G_{0,m}^{cl}$ is discrete, with the number of poles determined by the cluster size.

The impurity Hamiltonian for the cluster is defined as:

$$\begin{aligned} H = & \sum_{m\sigma} (\varepsilon_m - \mu) n_{m\sigma} + \sum_{k\sigma} \varepsilon_k n_{k\sigma} \\ & + \sum_{mk\sigma} V_{mk} [c_{m\sigma}^\dagger c_{k\sigma} + \text{H.c.}] \\ & + \sum_m U n_{m\uparrow} n_{m\downarrow} + \sum_{m < m' \sigma \sigma'} (U' - J \delta_{\sigma\sigma'}) n_{m\sigma} n_{m'\sigma'} \\ & - \sum_{mm'} J' [c_{m\uparrow}^\dagger c_{m\downarrow}^\dagger c_{m'\downarrow}^\dagger c_{m'\uparrow} + c_{m\uparrow}^\dagger c_{m\downarrow}^\dagger c_{m'\uparrow} c_{m'\downarrow}] \end{aligned} \quad (7)$$

where $c_{m\sigma}^{(+)}$ are annihilation (creation) operators for electrons in impurity level $m \leq 3$ with spin σ and $n_{m\sigma} = c_{m\sigma}^\dagger c_{m\sigma}$, with a similar notation for the bath levels $k = 4 \dots n_s$. H.c. denotes Hermitian conjugate terms. The atomic part of the Hamiltonian is identical with the

atomic part of the Hamiltonian of the extended material. The intra- and inter-orbital impurity Coulomb energies are denoted by U and U' . The exchange integral is J . Because of rotational invariance it obeys the relation $U' = U - 2J$. Spin-flip and pair-exchange terms are denoted explicitly by J' . In the case of isotropic Hund exchange, one has $J' = J$. In the case of Ising-like exchange these terms are neglected, so that $J' = 0$.

Within the diagonal a_g, e'_g basis, the cluster Green's function has the spectral representation:^{1,28}

$$\begin{aligned} G_m^{cl}(i\omega_n) &= \frac{1}{Z} \sum_{\nu\mu} \frac{|\langle \mu | c_{m\sigma}^\dagger | \nu \rangle|^2}{E_\nu - E_\mu - i\omega_n} [e^{-\beta E_\nu} + e^{-\beta E_\mu}] \\ &= \frac{1}{Z} \sum_{\nu} e^{-\beta E_\nu} [G_{m\sigma}^{\nu+}(i\omega_n) + G_{m\sigma}^{\nu-}(i\omega_n)] \end{aligned} \quad (8)$$

where E_ν and $|\nu\rangle$ are eigenvalues and eigenvectors of the impurity Hamiltonian and $Z = \sum_{\nu} \exp(-\beta E_\nu)$ is the partition function. The excited state Green's functions are given by

$$G_{m\sigma}^{\nu+}(i\omega_n) = \sum_{\mu} \frac{|\langle \mu | c_{m\sigma}^\dagger | \nu \rangle|^2}{E_\nu - E_\mu - i\omega_n}, \quad (9)$$

$$G_{m\sigma}^{\nu-}(i\omega_n) = \sum_{\mu} \frac{|\langle \mu | c_{m\sigma} | \nu \rangle|^2}{E_\mu - E_\nu - i\omega_n}. \quad (10)$$

In analogy to Eq. (4) the cluster self-energy is given by the expression:

$$\Sigma_m^{cl}(i\omega_n) = G_{0,m}^{cl}(i\omega_n)^{-1} - G_m^{cl}(i\omega_n)^{-1}. \quad (11)$$

As will be discussed in more detail in Subsection C, it is useful to regard the self-energy as the central quantity determined via DMFT. The key physical assumption within the ED approach is then that the cluster self-energy is an adequate representation for the self-energy of the extended solid, i.e.,

$$\Sigma_m(i\omega_n) \approx \Sigma_m^{cl}(i\omega_n). \quad (12)$$

From Eq. (4) it now follows that

$$G_m(i\omega_n) \approx G_m^{cl}(i\omega_n). \quad (13)$$

The approximate equalities here are important since they ensure that, as in the case of $G_{0,m}$, at real ω two alternative representations exist: a continuous one for the lattice Green's function G_m and self-energy Σ_m , and a discrete one for the cluster Green's function G_m^{cl} and self-energy Σ_m^{cl} . (See Fig. 13 of Ref. 1 for a nice illustration of the fact that continuous and discrete real- ω spectra can nearly coincide at Matsubara frequencies.)

Transforming from the a_g, e'_g basis to the t_{2g} basis via $\Sigma_{ii} = \Sigma_{a_g} + 2\Sigma_{e'_g}$, $\Sigma_{i \neq j} = \Sigma_{a_g} - \Sigma_{e'_g}$, we insert this self-energy into the solid Green's function Eq. (1). The iteration cycle then has the schematic form:

$$\Sigma \rightarrow G \rightarrow G_0 \approx G_0^{cl} \rightarrow G^{cl} \rightarrow \Sigma^{cl} \approx \Sigma. \quad (14)$$

This procedure is repeated until a self-consistent solution is found for a given chemical potential. This potential is then varied until the calculated total occupancy of the t_{2g} bands agrees with the desired occupancy.

In practice, we start from the non-interacting case, where the cluster levels ε_m and ε_k and hopping matrix elements V_{mk} are found for $G_{0,m}(i\omega_n) = G_m(i\omega_n)$ with $\Sigma_m = 0$. These cluster parameters are then used to begin the iteration at finite Coulomb and exchange energies for a given temperature. Finally, the spectral distributions are given by

$$A_m(\omega) = -\frac{1}{\pi} \text{Im} G_m(\omega). \quad (15)$$

The transformation of $G_m(i\omega_n)$ and $\Sigma_m(i\omega_n)$ to real frequencies will be discussed in the following subsection.

At low temperatures, the Boltzmann factors in Eq. (8) ensure that only a small number of excited states $|\nu\rangle$ are needed. Because of the sparseness of the impurity Hamiltonian matrix, these states can be evaluated exactly by using the Arnoldi algorithm.²⁹ For a given excited state the Green's functions $G_{m\sigma}^{\nu\pm}(i\omega_n)$ can then be calculated very accurately using the Lanczos procedure, by starting from the vectors $c_{m\sigma}^+|\nu\rangle$ and $c_{m\sigma}|\nu\rangle$, respectively:

$$G_{m\sigma}^{\nu+}(i\omega_n) = \frac{\langle \nu | c_{m\sigma} c_{m\sigma}^+ | \nu \rangle}{a_{0+} - i\omega_n + \frac{b_{1+}^2}{a_{1+} - i\omega_n + b_{2+}^2 / \dots}}, \quad (16)$$

$$G_{m\sigma}^{\nu-}(i\omega_n) = \frac{\langle \nu | c_{m\sigma}^+ c_{m\sigma} | \nu \rangle}{a_{0-} - i\omega_n + \frac{b_{1-}^2}{a_{1-} - i\omega_n + b_{2-}^2 / \dots}}. \quad (17)$$

The reformulation of the cluster Green's function in Eq. (8), (9), (10) is similar to the one used by Capone et al.²⁸ in the single-band case, except that these authors calculate the excited states $|\nu\rangle$ by applying the Lanczos method. This is faster than the exact solution if only few excited states are important. However, once extensive re-orthogonalization is required to obtain sufficiently accurate excited states, the Lanczos method becomes increasingly time-consuming so that the exact approach is preferable.

The Arnoldi algorithm is very useful since it enormously reduces both storage and time requirements to carry out ED/DMFT calculations. For $n_s = 12$ the largest Hilbert space for $n_\uparrow = n_\downarrow = 6$ has dimension $N = 853776$. Nevertheless, at most $M = 23$ elements are finite in any given row of the Hamiltonian matrix. The size of the effective $N \times M$ matrix is therefore less than for full diagonalization of the largest sector (4900) in the case $n_s = 8$. Moreover, at temperatures of about $T = 10$ meV fewer than 30 of the 169 possible $(n_\uparrow, n_\downarrow)$ configurations have lowest eigenvalues with Boltzmann factors larger than 10^{-5} . Most of these sectors contribute only few excited states. Only in some $(n_\uparrow, n_\downarrow)$ sectors 20 to 40 eigenstates are important. Thus for a total of about 300 excited states the Green's functions $G_{m\sigma}^{\nu\pm}(i\omega_n)$ are calculated via the Lanczos procedure. Of course, this number

increases at higher temperatures, and if Boltzmann factors smaller than 10^{-5} are included for higher precision. Finally, the Arnoldi algorithm requires as main computational step the matrix times vector operation $Hu = v$ where H has effective dimension $N \times M$, the vectors u, v are of length N and the internal sum extends only over the finite elements of H . Thus, in contrast to full diagonalization, this method is ideally suited for parallelization. Using 16 processors one iteration step takes less than 30 Min.

We have tested the above procedure on the two-band model consisting of half-filled subbands of different widths and found excellent agreement with previous results for $n_s = 8$ based on full diagonalization.¹⁸

B. Quasi-particle spectra at real frequencies

In the ED/DMFT equations given above we explicitly distinguish, via the superscript cl , the cluster Green's functions and self-energy from the corresponding quantities of the extended solid. This is done in order to emphasize that ED/DMFT is well suited for evaluating continuous solid quasi-particle spectra at real frequencies, as we now explain.

The key point is that the solid spectra are to be derived from $G_m(\omega)$, Eq. (1), rather than $G_m^{cl}(\omega)$, Eq. (8). Although in the self-consistent limit both functions agree at Matsubara frequencies within some uncertainty determined by the cluster size, they differ fundamentally at real frequencies, with $G_m(\omega)$ exhibiting a smooth spectrum and $G_m^{cl}(\omega)$ consisting of δ functions. Within the spirit of finite-temperature ED/DMFT each iteration step involves the evaluation of the solid Green's function G_m via Eq. (1) and the subsequent approximation of the associated impurity function $G_{0,m}$ in Eq. (4) via the discrete cluster spectrum of $G_{0,m}^{cl}$, Eq. (6). At a given temperature, the quality of this projection onto the set of Matsubara frequencies depends strongly on the cluster size, i.e., on the number of poles at real ω .

The task at the end of the iteration procedure, of transforming the lattice subband Green's functions $G_m(i\omega_n)$ from Matsubara frequencies to real ω , is therefore similar to the one faced in QMC/DMFT. The difference is that the ED/DMFT data exhibit finite-size effects rather than statistical uncertainties.

Since the ED/DMFT calculations are free of statistical effects, a convenient extrapolation of $G_m(i\omega_n)$ to real frequencies can be achieved by using, for example, the routine *ratint*³⁰ based on an approximation in terms of rational functions. The polynomial basis of this extrapolation ensures that at real ω the correct continuous lattice spectrum is found for $\text{Im} G_m(\omega)$, rather than a discrete spectrum for fixed n_s , as obtained by fitting $G_{0,m}$ via the cluster impurity Green's function $G_{0,m}^{cl}$. We use the extrapolation routine *ratint* in the next section to evaluate the subband quasi-particle spectra $A_m(\omega)$ for $\text{Na}_{0.3}\text{CoO}_2$.

C. Central role of self-energy

We like to point out that, rather than back-transforming the lattice Green's function from imaginary to real frequencies, it is more appropriate to perform this transformation on the self-energy. In fact, the self-energy may be regarded as the central quantity determined by the DMFT self-consistent quantum-impurity treatment. Since ultimately one is interested in the solid quasi-particle Green's function given in Eq. (1), the single-particle features determined by the Hamiltonian $H(\mathbf{k})$ can evidently be evaluated at real ω . Thus, only the real- ω variation of the self-energy is needed. As a result, \mathbf{k} -resolved spectra can be calculated via

$$A(\mathbf{k}, \omega) = -\frac{1}{\pi} \text{Im Tr} \left(\omega + \mu - H(\mathbf{k}) - \Sigma(\omega) \right)^{-1}. \quad (18)$$

The usefulness of transforming Σ from Matsubara to real frequencies can be seen at small U . The spectral details of G are then almost entirely of single-particle character, whereas the self-energy becomes very smooth. Since Σ is a highly convoluted function, with contributions stemming from the occupied and unoccupied regions of the density of states, back-transforming it to real ω becomes progressively simpler at small U . In contrast, the back-transformation of G gets more difficult. Obviously, since $H(\mathbf{k})$ is known the back-transformation of the single-particle part of G can be avoided altogether.

It is well known also that different cluster properties exhibit different convergence with increasing cluster size. Single-particle features, such as the local density of states at the impurity in a given energy window, converge most slowly. Integrated properties, such as the total energy, converge more rapidly. Since the phase space for two-particle interactions increases extremely fast with cluster size, many-body properties such as the self-energy exhibit even more favorable convergence properties. On the other hand, the cluster Green's function involves both single-electron and many-electron features. Only the latter converge rapidly with cluster size. These different behaviors also suggest that it is useful to regard $\Sigma \approx \Sigma^{\text{cl}}$ as the key quantity derived within ED/DMFT.

To extrapolate $\Sigma_m(i\omega_n)$ to real frequencies it is first necessary to remove the Hartree-Fock limit given by $\Sigma_m^{\text{HF}}(i\omega_n) = \Sigma_m(i\omega_n \rightarrow \infty)$. The remainder can then be transformed to real ω by using the same extrapolation routine *ratint* as for the derivation of $G_m(\omega)$.³¹ As in the latter case, this routine ensures that the correct continuous lattice self-energy is found, rather the discrete version appropriate for the cluster self-energy. Since back-transformation of single-particle features is avoided, and quasi-particle features are calculated from Eq. (1) at real ω , finer spectral details are retained than when $G_m(i\omega_n)$ is transformed to the real axis. Nevertheless, in the following section we show that both schemes yield consistent spectra.

Before closing this section we note that the back-transformation of the self-energy from Matsubara to real

frequencies should also be useful within QMC/DMFT. By viewing QMC as a tool for evaluating Σ , the same separation of many-body features from single-particle aspects can be achieved if quasi-particle spectra are evaluated from Eq. (1) at real ω . Of course, the statistical uncertainties associated with QMC make the transformation of $\Sigma(i\omega_n)$ more subtle than in the present ED case. Nevertheless, after subtraction of the Hartree-Fock limit from the real part of Σ , and after proper normalization (determined by the asymptotic behavior of the imaginary part), the use of the maximum entropy method on $\Sigma(i\omega_n)$, $\Sigma(\tau)$ should be more accurate than on $G(i\omega_n)$, $G(\tau)$, since the back-transformation of single-particle features is avoided.

III. APPLICATION TO $\text{Na}_{0.3}\text{CoO}_2$

We have applied the multi-band ED/DMFT approach discussed in the previous section to investigate the correlation induced charge transfer between t_{2g} bands of $\text{Na}_{0.3}\text{CoO}_2$. The controversial small Fermi surface pockets arise from e'_g bands that extend less than 100 meV above E_F . Since onsite Coulomb energies are much larger than the t_{2g} band width, it is important to inquire whether correlations can lead to a filling of the e'_g bands.

The single-particle properties for this Na concentration were derived from a full-potential linear augmented plane wave (LAPW) calculation, which was then fitted to a 3×3 t_{2g} tight-binding Hamiltonian including three neighboring shells and $dd\sigma$, $dd\pi$ and $dd\delta$ matrix elements. Further details concerning the LDA band structure are given in Ref.²³.

For the combined t_{2g} and e_g bands of $\text{Na}_{0.3}\text{CoO}_2$ U was calculated to be about 3.7 eV.³² For the t_{2g} subbands a smaller value might be appropriate to account for screening via e_g electrons. Since precise values of U and J are not known, ED/DMFT calculations up to $U = 5$ eV were carried out, assuming $J = U/4$.

Fig. 1 shows the Co a_g and e'_g subband self-energies $\Sigma_m(i\omega_n)$ for $U = 3$ eV and $J = 0.75$ eV at $T = 10$ meV. Hund exchange is fully included, i.e., $J' = J$. As a result of the large cluster size the spacing between excited states of the impurity Hamiltonian is less than 0.001 eV. Although each impurity orbital hybridizes only with three bath levels, the Coulomb and exchange interactions at the impurity site induce coupling between all bath levels, so that the excited states of the total cluster are significantly more closely spaced than for $n_s = 4$ in the single-band case. Thus, even at temperatures as low as $T = 2.5$ meV finite-size effects are extremely small. The slight differences of the real part of the self-energy are related to the temperature dependence of the chemical potential.

The a_g and e'_g quasi-particle weights $Z_m = 1/[1 - d\text{Re}\Sigma_m(\omega)/d\omega] \approx 1/[1 - \text{Im}\Sigma_m(i\omega_0)/\omega_0]$ derived from these self-energies are $Z_{a_g} \approx 0.52$ and $Z_{e'_g} \approx 0.62$, giving

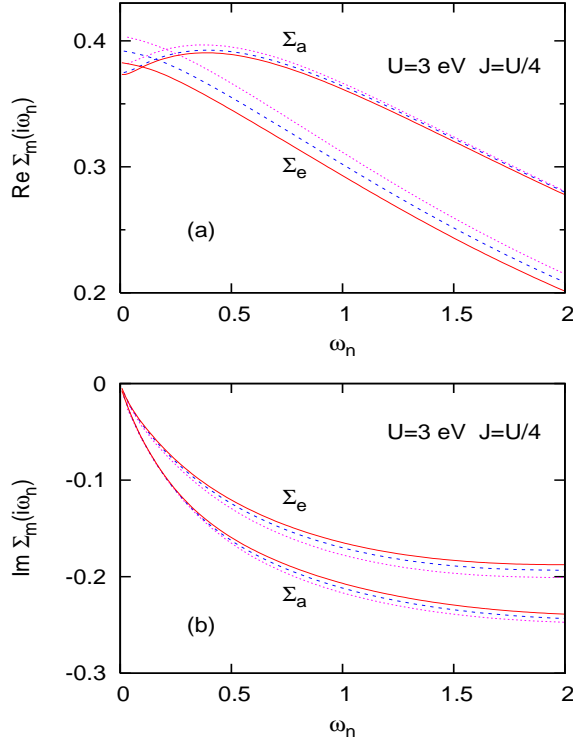


FIG. 1: Subband self-energies $\Sigma_m(i\omega_n)$ of $\text{Na}_{0.3}\text{CoO}_2$ as calculated within ED/DMFT for $U = 3.0$ eV, $J = 0.75$ eV at several temperatures: red curves: $T = 2.5$ meV, blue curves: $T = 5$ meV, magenta curves: $T = 10$ meV. The Hartree-Fock limit is subtracted from $\text{Re} \Sigma_m(i\omega_n)$.

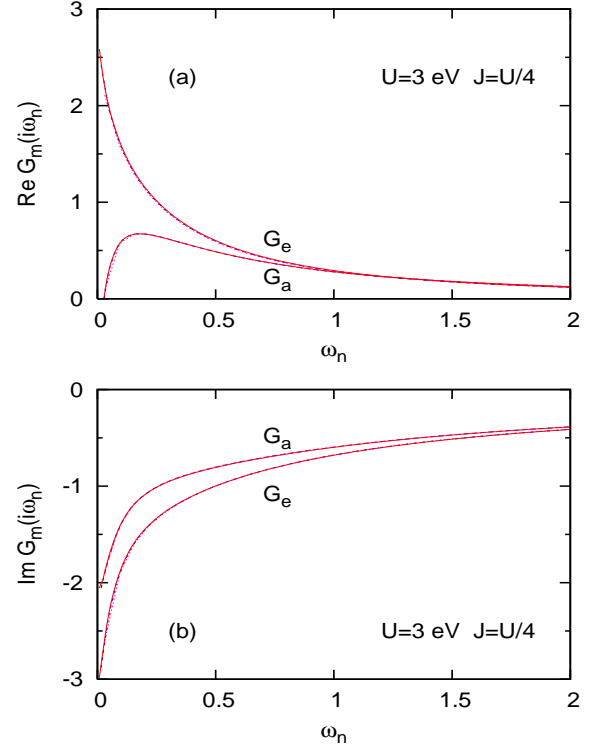


FIG. 2: Subband Green's functions $G_m(i\omega_n)$ of $\text{Na}_{0.3}\text{CoO}_2$ for $U = 3.0$ eV, $J = 0.75$ eV, at several temperatures: red curves: $T = 2.5$ meV, blue curves: $T = 5$ meV, magenta curves: $T = 10$ meV.

effective masses $m_{a_g}^* \approx 1.9$ and $m_{e'_g}^* \approx 1.6$, respectively.

The corresponding subband lattice Green's functions are plotted in Fig. 2 for the same parameters as in Fig. 1. As in the case of the self-energies, the distributions are very smooth and exhibit only very small deviations caused by finite-size effects.

Fig. 3 shows the variation of the a_g and e'_g occupations with onsite Coulomb energy at $T = 10$ meV. Both isotropic Hund exchange ($J' = J$) and Ising exchange ($J' = 0$) are seen to give nearly identical charge transfer from e'_g to a_g bands. In the present ED/DMFT treatment this transfer is slightly less pronounced than the one found within QMC/DMFT for Ising exchange at higher T ,²³ but the trends in both DMFT calculations are consistent. Thus, both DMFT treatments suggest that local Coulomb correlations stabilize the e'_g Fermi surface pockets. The overall topology of the Fermi surface therefore remains the same as predicted by the LDA, i.e., correlation effects cannot explain the absence of the e'_g pockets from the ARPES data.

Note that up to $U = 5$ eV the subband occupations show no sign of any reversal of charge transfer. The opposite result found using the Gutzwiller approach²⁶ in the $U = \infty$ limit might therefore be a consequence of the approximate treatment of dynamical correlations. In this

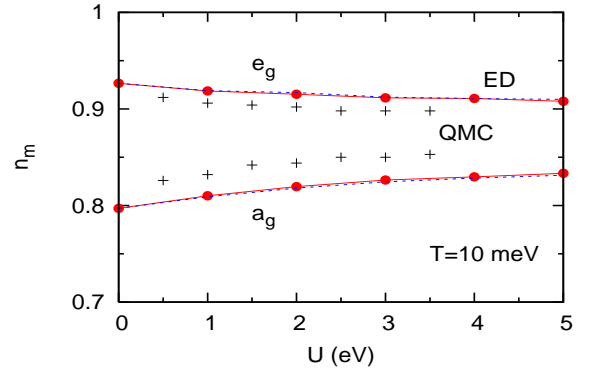


FIG. 3: Subband occupations n_{a_g} and $n_{e'_g}$ (per spin band) of $\text{Na}_{0.3}\text{CoO}_2$ as a function of U , with $J = U/4$ at $T = 10$ meV. Solid (red) curves: Hund exchange $J' = J$, dashed (blue) curves: Ising exchange $J' = 0$. The corresponding QMC/DMFT results²³ for $T = 30 \dots 60$ meV are indicated by the symbols (+). The total occupation is $2n_{a_g} + 4n_{e'_g} = 5.3$.

scheme the true complex frequency dependent self-energy is replaced by real coefficients representing the shift and narrowing of subbands.

Fig. 4 shows the frequency variation of the subband self-energies, as obtained directly from $\Sigma_m(i\omega_n)$ via the

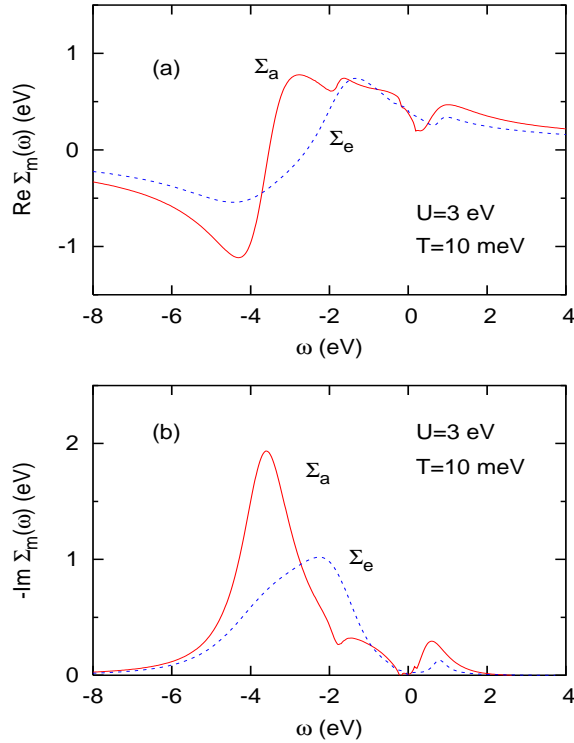


FIG. 4: Subband self-energies $\Sigma_m(\omega)$ of $\text{Na}_{0.3}\text{CoO}_2$ at real frequencies, for the same parameters as in Fig. 1. Solid (red) curves: a_g bands, dashed (blue) curves: e'_g bands. (a) $\text{Re}\Sigma_m(\omega)$; (b) $-\text{Im}\Sigma_m(\omega)$. The Hartree-Fock limit is subtracted from the real part.

extrapolation routine *ratint*. The Kramers-Kronig relations between the real and imaginary parts of $\Sigma_m(\omega)$ are very well satisfied. The striking asymmetry between the negative and positive frequency regions is a consequence of the near filling of the subbands.

As pointed out in the previous section, quasi-particle spectra at real frequencies can be derived by back-transforming the solid Green's function $G_m(i\omega_n)$, or by first transforming $\Sigma_m(i\omega_n)$ and then applying Eq. (1) at real ω . The comparison shown in Fig. 4 proves that both methods are consistent, and that the latter scheme retains finer spectral details originating from the single-particle Hamiltonian. For instance, the e'_g spectrum obtained via Eq. (1) and $\Sigma_m(\omega)$ shows two peaks below E_F which evidently are the shifted and broadened density of states features near 0.4 and 0.8 eV below the Fermi level. Also, the peak close to E_F exhibits some of the fine structure of the single-particle density of states. These details are lost if the spectrum is instead derived via back-transformation of $G_m(i\omega_n)$.

Interestingly, the a_g spectrum has a steep positive slope at E_F , while the e'_g spectrum has a strong negative slope. This holds true for both methods of evaluating the real frequency spectra. Also, the a_g quasi-particle spectrum exhibits a pronounced minimum at about 0.1 eV be-

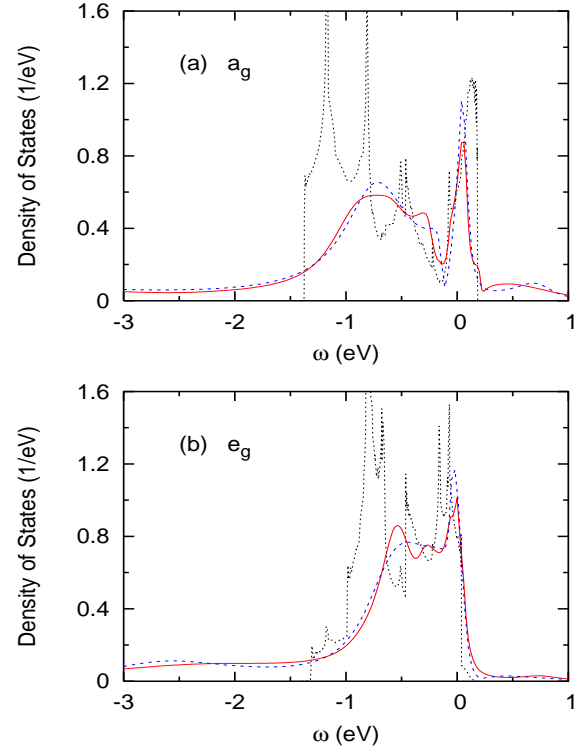


FIG. 5: Quasi-particle spectra of (a) a_g and (b) e'_g subbands of $\text{Na}_{0.3}\text{CoO}_2$, calculated within ED/DMFT for the same parameters as in Fig. 1. Solid (red) curves: spectra derived from $G_m(\omega)$ via $\Sigma_m(\omega)$; dashed (blue) curves: spectra obtained by extrapolating $G_m(i\omega_n)$ to real ω ; dotted (black) curves: single-particle density of states.

low E_F . This feature exists already in the single-particle density of states and is evidently not obliterated by correlation effects.

Both subbands exhibit the usual correlation induced band narrowing, quasi-particle damping, and incoherent spectral weight in the region below the bottom of the bands, associated with Hubbard peaks. Qualitatively, these spectra agree with the ones derived previously using the QMC/DMFT and the maximum entropy method.^{23,24,25}

For comparison with these lattice spectra we show in Fig. 5 the cluster spectra obtained by evaluating Eq. (8) at $\omega + i\delta$ instead of $i\omega_n$. Because of the large cluster size, the level spacing between excited states in the metallic phase of $\text{Na}_{0.3}\text{CoO}_2$ is less than 10^{-3} eV. Thus, with only a minor broadening these cluster spectra look very smooth indeed. The spectral weight is located mainly in the t_{2g} band region, and there is clear evidence of incoherent weight associated with Hubbard bands. Both the a_g and e'_g spectral distributions exhibit three main features in the band region, as in the case of the bare density of states. Nevertheless, these features are much narrower than in the corresponding lattice spectra shown in Fig. 4. This is not surprising since, as pointed out in

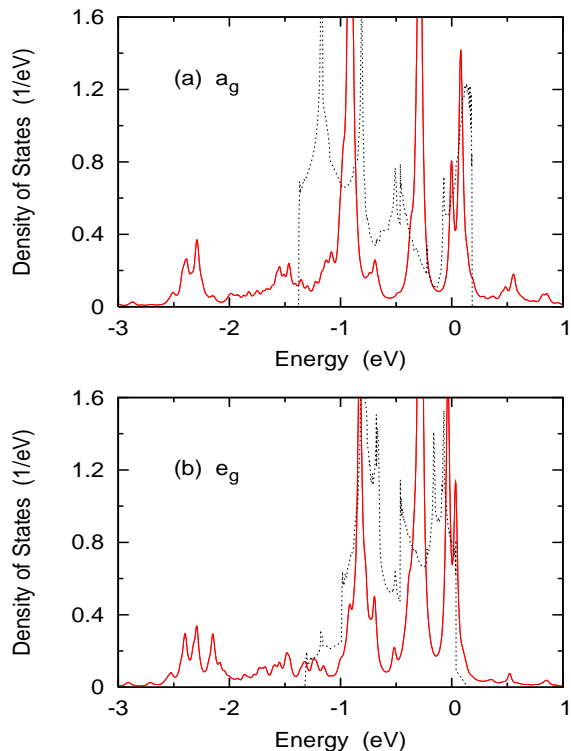


FIG. 6: Cluster spectra of (a) a_g and (b) e'_g orbitals of $\text{Na}_{0.3}\text{CoO}_2$, as calculated from Eq. (8). Solid (red) curves: $-\text{Im } G_m^{\text{cl}}(\omega + i\delta)$ with $\delta = 25$ meV; dotted (black) curves: single-particle density of states.

the previous section, the cluster Green's function depends on single-particle and many-body aspects. Only the latter, represented by the self-energy, converge rapidly with cluster size. Thus, increasing the artificial broadening of the cluster spectra does not yield the lattice spectra. Cluster spectra would resemble more closely those of the solid only if n_s is significantly increased. To analyze photoemission spectra of the solid material, Eq. (1) should therefore be used at real ω rather than Eq. (8).

Transforming the subband self-energies $\Sigma_{a_g}(\omega)$ and $\Sigma_{e'_g}(\omega)$ to the t_{2g} basis, they can be used to evaluate the momentum dependence of the quasi-particle band structure, as indicated in Eq. (18). This is shown in Fig. 7 for the ΓK and ΓM symmetry directions of the hexagonal Brillouin Zone. The e'_g Fermi surface pockets are associated with the flat bands reaching just above E_F along ΓK . The maximum of this band is barely shifted, but the crossing of E_F occurs slightly farther away from the maximum, leading to a weak enlargement of the hole pocket. Conversely, the diameter of the large a_g pocket centered at Γ is slightly reduced.

These results demonstrate that, although correlation effects induce band narrowing and broadening, they do not alter the basic dispersion of the t_{2g} bands of $\text{Na}_{0.3}\text{CoO}_2$. In particular, it does not seem possible to interpret these bands in terms of a single-band model,

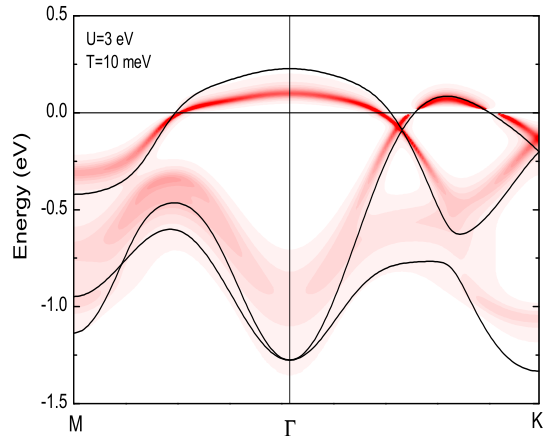


FIG. 7: Dispersion of quasi-particle bands of $\text{Na}_{0.3}\text{CoO}_2$ along $\text{M}\Gamma$ and ΓK for $T = 10$ meV. The LDA bands derived from $H(\mathbf{k})$ are denoted by the solid lines.

with a flat a_g band limited to within a very narrow energy range near E_F .^{34,35}

IV. SUMMARY AND OUTLOOK

We have applied ED/DMFT to investigate the correlation induced charge transfer between the t_{2g} bands in $\text{Na}_{0.3}\text{CoO}_2$. Since previous QMC/DMFT studies of this problem were limited to Ising exchange the role of full Hund's coupling had remained unresolved. The ED calculations show that the charge transfer follows the same trend for both Hund and Ising exchange: The e'_g bands donate some of their charge to the a_g bands, i.e., the e'_g Fermi surface hole pockets are slightly enlarged. These ED results fully confirm the trend obtained previously within QMC/DMFT for Ising exchange. Thus, local Coulomb correlations cannot explain the absence of these pockets from the ARPES data.

These results suggest that ED/DMFT is a useful method for the study of strongly correlated three-band systems. By exploiting the sparseness of the impurity Hamiltonian the cluster size $n_s = 12$ can now be investigated, without loss of accuracy, with about the same computational effort as $n_s = 8$ using full diagonalization. The large cluster size ensures that the level spacing among excited states is very small, so that finite-size effects are greatly reduced.

In view of this improvement, ED/DMFT can now be regarded as complementary to QMC/DMFT. We point out, however, that in comparison to standard QMC/DMFT based on the Hirsch-Fye algorithm, the ED/DMFT approach is free of sign problems. Thus, complete Hund exchange and large on-site Coulomb interactions can be treated. In addition, very low temperatures

can be reached. In principle, results for $T \rightarrow 0$ can also be generated within ED/DMFT. This limiting region, however, requires special care since certain system properties might be sensitive to remaining finite-size effects even for $n_s = 12$.

We have also demonstrated that ED/DMFT provides continuous quasi-particle spectra and self-energies of the extended solid at real frequencies. Moreover, by considering the self-energy as the principal quantity derived within DMFT, a clear separation of single-electron and many-body aspects in spectral distributions can be achieved.

In the future it should be valuable to apply ED/DMFT to other multi-band materials that have so far been studied only within Ising exchange and QMC/DMFT, but where full Hund's coupling is crucial. Also, by exploit-

ing the fact that the present scheme can easily be parallelized, much larger cluster sizes are feasible. This opens the path for the study of various other material properties, including non-local effects.

Acknowledgements: We like to thank Eric Koch for drawing our attention to the Arnoldi algorithm. We also thank him and Theo Costi for stimulating discussions. Most of the ED/DMFT calculations were carried out on the IBM supercomputer (JUMP) of the Forschungszentrum Jülich.

E-mail: a.perroni@fz-juelich.de; ishida@chs.nihon-u.ac.jp; a.liebsch@fz-juelich.de

-
- ¹ For a review of early work, see: A. Georges, G. Kotliar, W. Krauth and M. J. Rozenberg, *Rev. Mod. Phys.* **68**, 13 (1996).
 - ² For recent reviews, see: K. Held, *cond-mat/0511293*; A. Georges *et al.*, *cond-mat/0403123*; G. Kotliar and S. Savrasov, *cond-mat/0208241*.
 - ³ M. Imada, A. Fujimori, and Y. Tokura, *Rev. Mod. Phys.* **70**, 1039 (1998).
 - ⁴ K. G. Wilson, *Rev. Mod. Phys.* **47**, 773 (1975).
 - ⁵ M. Caffarel and W. Krauth, *Phys. Rev. Lett.* **72**, 1545 (1994).
 - ⁶ J. E. Hirsch and R. M. Fye, *Phys. Rev. Lett.* **56**, 2521 (1986).
 - ⁷ L. Craco, M. S. Laad, and E. Müller-Hartmann, *Phys. Rev. Lett.* **90**, 237203 (2003).
 - ⁸ M. I. Katsnelson and A. I. Lichtenstein, *Eur. Phys. J. B* **30**, 9 (2002).
 - ⁹ For a discussion of this problem, see: K. Held and D. Vollhardt, *Eur. Phys. J. B* **5**, 473 (1998).
 - ¹⁰ R. Arita and K. Held, *Phys. Rev. B* **72**, 201102 (2005).
 - ¹¹ A. Koga, N. Kawakami, T. M. Rice, and M. Sigrist, *Phys. Rev. B* **72**, 045128 (2005).
 - ¹² A. N. Rubtsov, V. V. Savkin and A. I. Lichtenstein, *Phys. Rev. B* **72**, 035122 (2005).
 - ¹³ See also: Ph. Werner, A. Comanac, L. de' Medici, M. Troyer, and A. J. Millis, *Phys. Rev. Lett.* **97**, 076405 (2006).
 - ¹⁴ S. Sakai, R. Arita, K. Held, and H. Aoki, *cond-mat/605526*.
 - ¹⁵ A. Koga, N. Kawakami, T. M. Rice and M. Sigrist, *Phys. Rev. Lett.* **92**, 216402 (2004).
 - ¹⁶ A. Liebsch, *Phys. Rev. Lett.* **95**, 116402 (2005).
 - ¹⁷ S. Biermann, L. de' Medici, and A. Georges, *Phys. Rev. Lett.* **95**, 206401 (2005).
 - ¹⁸ A. Liebsch and T. A. Costi, *Eur. Phys. J. B* **51**, 523 (2006).
 - ¹⁹ K. Takada *et al.*, *Nature* **422**, 53 (2003); R. E. Schaak *et al.*, *Nature* **424**, 527 (2003).
 - ²⁰ M. Jarrell and J. E. Gubernatis, *Phys. Rep.* **269**, 133 (1996).
 - ²¹ D. J. Singh, *Phys. Rev. B* **61**, 13397 (2000).
 - ²² H. B. Yang *et al.*, *Phys. Rev. Lett.* **95**, 146401 (2005); *Phys. Rev. Lett.* **92**, 246403 (2004); M. Z. Hasan *et al.*, *Phys. Rev. Lett.* **92**, 246402 (2004); T. Shimojima *et al.*, *cond-mat/0606424*.
 - ²³ H. Ishida, M. Johannes, and A. Liebsch, *Phys. Rev. Lett.* **94**, 196401 (2005).
 - ²⁴ F. Lechermann, S. Biermann, and A. Georges, *Progr. Th. Phys. Suppl. No.160*, p. 233 (2005).
 - ²⁵ C. A. Marianetti and G. Kotliar, *cond-mat/0605177*.
 - ²⁶ S. Zhou, *et al.*, *Phys. Rev. Lett.* **94**, 206401 (2005).
 - ²⁷ D. J. Singh and D. Kasinathan, *Phys. Rev. Lett.* **97**, 016404 (2006).
 - ²⁸ M. Capone, L. de' Medici, and A. Georges, *cond-mat/0512484*.
 - ²⁹ R. B. Lehoucq, D. C. Sorensen, and C. Yang, *ARPACK Users' Guide* (1997).
 - ³⁰ *Numerical Recipes in Fortran 77*, Cambridge University Press, p. 106 (1986-1992).
 - ³¹ We focus here on the metallic phase. Near a metal insulator transition, the singular part of the self-energy has to be treated separately.
 - ³² M. D. Johannes, I. I. Mazin, and D. J. Singh, *cond-mat/0408696*.
 - ³³ L. Balicas *et al.*, *Phys. Rev. Lett.* **97**, 126401 (2006).
 - ³⁴ J. Merino, B. J. Powell, and R. H. McKenzie, *Phys. Rev. B* **73**, 235107 (2006).
 - ³⁵ D. Qian *et al.*, *Phys. Rev. Lett.* **96**, 216405 (2006).